3D-printed hierarchical pillar array electrodes for high performance semi-artificial photosynthesis

Xiaolong Chen[1], Joshua M. Lawrence[2], Laura T. Wey[2], Lukas Schertel[1], Qingshen Jing[3], Silvia Vignolini[1], Christopher J. Howe[2], Sohini Kar-Narayan[3], Jenny Z. Zhang[1*]

[1] Yusuf Hamied Department of Chemistry, University of Cambridge, Lensfield Road, Cambridge CB2 1EW, UK;

[2] Department of Biochemistry, University of Cambridge, Tennis Court Road, Cambridge, CB2 1QW, UK;

[3] Department of Materials Science and Metallurgy, University of Cambridge, 27 Charles Babbage Road, Cambridge, CB3 0FS, UK;

[*] To whom correspondence may be addressed. Email: jz366@cam.ac.uk.

Abstract

The re-wiring of photosynthetic bio-machineries to electrodes is a forward-looking semi-artificial route for sustainable bio-electricity and fuel generation. Currently, it is unclear how the electrode and bio-material interface can be designed to meet the complex requirements for high bio-photoelectrochemical performance. Here, we developed an aerosol jet printing method for generating hierarchical electrode structures using indium tin oxide nanoparticles. We printed libraries of micropillar array electrodes varying in height and sub-micron surface features and studied the energy/electron transfer processes across the bio-electrode interfaces. When wired to the cyanobacterium *Synechocystis* sp. PCC 6803, micropillar array electrodes with micro-branches exhibited favourable biocatalyst loading, light utilisation and electron flux output, ultimately almost doubling the photocurrent of state-of-the-art porous structures of the same height. When the micropillars' heights were increased to 600 μm, milestone mediated photocurrent densities of 245 μA cm^{-2} (the closest thus far to theoretical predictions) and external quantum efficiencies of up to 29% could be reached. This study demonstrates how bioenergy from photosynthesis could be more efficiently harnessed in the future and provide new tools for 3D electrode design.

Introduction

Biocatalysts (from enzymes to living microorganisms) can be electrochemically connected (wired) to electrodes for biotechnological applications or fundamental studies[1-4]. In particular, cyanobacteria (photosynthetic bacteria) are free-living, self-repairing, abundant, solar-powered

biocatalysts that can be wired to electrodes for electricity generation (biophotovoltaics, **Fig. 1 a-b**) and chemical synthesis[2,5-7].

Presently, semi-artificial approaches for solar energy conversion are in the nascent phase, and photocurrent densities achievable by cyanobacterial electrodes have been calculated to be between 340 µA cm^{-2} and 2400 µA cm^{-2} (at the lower estimate, the energy conversion efficiency compares favourably to that of industrial bio-fuel production)[8]. However, typical photocurrents generated by cyanobacterial-electrodes are two orders of magnitude below this value. This is despite substantial bioengineering efforts[9,10] to increase biological electron output and the deployment of artificial electron mediators, which can be introduced to maximise electron harvesting from the photosynthetic electron transport chain (**Fig. 1 b**)[6,8]. The bottleneck in current output likely lies with the electrode itself.

In photoelectrochemical reactions, the electrode structure must balance several factors to minimise reaction bottlenecks[11]. Where biocatalysts are employed, it must compensate for the larger catalyst dimensions and lower overall loading[2,6,12]. The state-of-the-art electrode architecture in both protein-film and biofilm photoelectrochemistry is the inverse opal (IO) porous structure[13] which has been fabricated from a variety of metal oxides[12,14-17]. In particular, indium-tin oxide (ITO) exhibits appropriate inertness, conductivity, light scattering, and biocompatibility properties[12]. It was demonstrated that the combination of the macro-porous structures (offering a large electroactive surface area and aiding biocatalyst penetration) with a meso substructure (aiding biocatalyst adhesion)[7,18] in a hierarchical architecture was important for efficient biocatalyst wiring[19]. When cells of the model cyanobacterium, *Synechocystis* sp. PCC 6803 (*Synechocystis*), were immobilised onto IO-ITO electrodes, a mediated photocurrent density of 14 µA cm^{-2} (**Fig. 1c**) and external quantum efficiency (EQE) of 2.7% were observed[7]. It is uncertain where the bottleneck in photocurrent lies (see **Supplementary Note 1**). Further progress in electrode design has been limited by the lack of versatile fabrication techniques that can generate large libraries of hierarchical electrode structures.

Here, we developed an aerosol jet printing method for the efficient and reproducible fabrication of large libraries of micropillar electrodes made from ITO nanoparticles. We demonstrated that this printing method could produce tuneable hierarchical features spanning five orders of magnitude in length scales in one printing step. This enabled us to fabricate libraries of hierarchical micropillar array electrodes (see **Supplementary Note 1**)[24,25] using ITO

nanoparticles (**Fig. 1 d-f**) that is not possible using other fabrication methods. We varied the heights and surface roughness of the pillars to tune the electroactive surface areas on multiple length scales and compared their properties against state-of-the-art IO-ITO electrodes. Using this approach, we expanded current understandings of electrode structure-activity relationships and arrived at a new generation of high-performing photosynthetic electrodes (**Fig. 1c**).

Aerosol jet printed ITO electrodes

Aerosol jet printing is an additive manufacturing technique that can print metal nanoparticle inks (**Fig. 2a**) with high design flexibility, resolution, and material deposition precision[26-30] via a contactless direct write approach[31-34]. However, the fabrication of 3D hierarchical structures using this technique has not been reported. To establish an aerosol jet printing method for the fabrication of 3D structures using an ITO nanoparticle ink, significant deviations from classical ink compositions and printing parameters were needed (**Fig. 2**; see **Supplementary Note 2** for a tutorial explanation of aerosol jet printing).

To produce pillar structures, a new parameter - the gas focussing pressure ratio, which is the balance between the pressure of the carrier gas and the sheath gas, was tuned (**Fig. 2b**). It was observed that at ratios of between 2.4 and 3.5, pillars of up to 800 µm could be printed. Below this range, insufficient materials would be deposited; above this range, an 'overspill' effect occurred, resulting in a thick unstable pillar base (**Fig. 2b inset**).

We endowed the printed pillars with micro-scale roughness by changing to non-classical co-solvent systems, such as water (non-volatile) and methanol (volatile), in the ink precursor. The ratio of the water to methanol was varied to result in aerosol streams of different droplet sizes and volatilities (see **Table S1**); high water content (>50% v/v) gave rise to 'droplet-like' features (**Fig. S1a)**; a methanol content of 50-65% v/v gave rise to 'smooth' nanoporous pillars (**Fig. 2d**, **Fig. S1b**); a methanol content of 65-75% v/v gave rise to sub-micron sized branched features (**Fig. 2e**); at a methanol content of >75% v/v, the diameter of the pillar became thin and brittle (**Fig. S1c**). The microbranches formed during the printing of the pillars was attributed to formation of smaller aerosol droplets at higher methanol contents. The small

droplets near the sheath gas interface were too small to resist the turbulence at the side of the deposited area and were further broken up at the turbulent front. The submicron droplets formed follow wide trajectory patterns to result in the branched features with the volatility of the co-solvent mixture aiding rapid solidification of the structure.

We identified ideal conditions for generating arrays of well-formed smooth micropillars of ITO nanoparticles (SP-ITO, **Fig. 2d**) and branched micropillars of ITO nanoparticles (BP-ITO, **Fig. 2e**), and electrodes varying in pillar height (50-800 µm) and roughness were printed for this study (**Fig. 1d** & **Fig. S2**). The conditions used for the printing of the micropillar electrodes (20 µm diameter, 50-800 µm height, 100 µm centre-to-centre spacing) are documented in **Table. S2**.

Characterization of the printed micro-pillar electrodes

The printed micropillar electrodes were annealed and confirmed to retain the ITO composition via energy-dispersive X-ray spectroscopy (**Fig. S3**). Scanning electron microscopy (SEM) images of the libraries of the annealed SP-ITO and BP-ITO structures showed that the printed pillars within each array were uniform in height and diameter. We observed that the branching decreased with the height of the BP-ITO structure, with reduced branching at the top half of pillars at heights > 400 µm (**Fig. S2**). This was attributed to the decrease in turbulence during the printing process as the distance between the printer nozzle and the tip of the pillar decreased.

The optical properties of the printed micropillar electrodes bare (in air) were measured with the aid of an integrating sphere (**Fig. S4 - S6**) and compared against benchmark third-generation IO-ITO electrodes (10 µm in pore size, 50 µm in height, **Fig. S7**), shown in **Fig. 3a-d**. We observed that when irradiated with 0° vertical incident white light (1 mW cm^{-2}), the bare IO-ITO structure transmitted 4.4 ± 2.0% and reflected 12.4 ± 1.6% of the incident light; the SP-ITO array structure of the same height transmitted 32.5 ± 0.7 % and reflected 15.6 ± 1.0% of the incident light, whereas the BP-ITO array structure transmitted 26.4 ± 2.1% and reflected 20.2 ± 2.2% of the incident light (**Fig. 3c**). As such, micropillar structures exhibited significantly enhanced light transmission ($p \leq 1.6 \times 10^{-3}$) compared to IO-ITO, with BP-ITO also exhibiting enhanced scattering ($p = 3.2 \times 10^{-2}$). From this, it could be predicted that much greater light harvesting by the *Synechocystis*-loaded electrodes is possible with the

micropillar micro-branched structures. The remainder of the incident light could be attributed to light absorbance by the material or loss from in plane scattering. This was much higher for the IO-ITO structure (83.2 ± 2.6%) than for the SP-ITO (51.9 ± 0.3%) and BP-ITO structures (53.3 ± 3.8%, $p \leq 2.5 \times 10^{-3}$) (**Fig. S8**).

SP-ITO and BP-ITO electrodes ranging from 50 µm to 800 µm in height (such heights were not accessible for IO-ITO) were also characterised. The transmittance of the bare SP-ITO and BP-ITO electrodes linearly decreased with the increase in height, which was partially due to the corresponding increase in thickness of the pillar base. The overall transmittance of SP-ITO was higher than that of BP-ITO because the micro-branches blocked approximately 8% of the incident light; similarly, the reflectance of BP-ITO was enhanced due to the increased scattering arising from the branch-like feature[35]. The reflectance was proportional to the height of the bare pillar structures (**Fig. 3c**).

The electrodes were incubated with a concentrated culture of *Synechocystis* (ca. 1.4 µm in diameter) for 12 h in the dark, gently rinsed, then immersed in aqueous BG11 medium for transmittance and reflectance measurements. Slight decreases in transmission and reflectance were observed for the *Synechocystis*-loaded IO-ITO electrodes (**Fig. 3d)**, which corresponds to a very small change in absorbance (<5%; **Fig. S8a**). However, in the presence of the adhered *Synechocystis* there was a significant decrease in the transmittance ($p \leq 3.7 \times 10^{-4}$) and reflectance ($p \leq 4.7 \times 10^{-3}$ f) of the taller (600 µm) micropillar electrodes (**Fig. 3d**). The presence of cells on the electrodes increased light absorption by up to 40% for the tallest pillar structures (**Fig. S8b**). This could be attributed to light absorption by the chlorophyll *a* (Chl *a*) and other pigments[36] which absorb light to drive photosynthesis.

The electroactive surface areas (EASAs) of the bare electrode structures were measured using capacitance measurements (**Fig. 3e** and **Fig. S9**). When structures of the same height (50 µm) and geometric area (0.0625 cm^2) were compared, IO-ITO had the highest EASA (0.24 ± 0.01 cm^2), followed by BP-ITO (0.19 ± 0.01 cm^2), then SP-ITO (0.160 ± 0.003 cm^2). The deviation of the measured EASA from the theoretical EASA (**Fig. S9b**) in the case of the IO-ITO is expected. Although regions of orderly IO-structures dominated, the electrode structure contained cracks (**Fig. S7**) and regions of heterogeneity which may be inaccessible to the electrolyte. In contrast, the theoretical EASAs of the micropillar electrodes matched almost exactly the experimentally measured values, which indicated that the electrolyte reached the entire printed structure and most of the ITO structure was electrochemically connected.

The cell loading capacity of each electrode structure was measured spectroscopically by assaying the Chl *a* content on the electrodes following experiments. With increasing pillar heights, higher total Chl *a* loading normalised by geometric area could be observed (**Fig. S10**); however, the relationship was not linear and **Fig. 3f** shows the Chl *a* loading density normalised by the electrode EASA. The micropillar electrodes exhibited comparable normalised cell loadings to IO-ITO at pillar heights 50 and 100 µm, with the BP-ITO structure at pillar height of 200 µm exhibiting the highest EASA-normalised cell density (3.69 ± 0.23 µg cm^{-2}), which was 60% higher in absorbed Chl *a* content compared to the IO-ITO electrode. The normalised Chl *a* content for the micropillar electrodes declined at heights above 200 µm - attributed to the decrease in micro-branching in the case of the BP-ITO and gravitational effects (cells settling on the base) limiting cell attachment at the pillar tops. Following cell immobilisation, the structures of the printed electrodes were observed to be unchanged (**Fig. S11-12**).

Confocal fluorescence microscopy was employed to acquire Z-stacks of the cell-loaded electrodes, exploiting the intrinsic fluorescence of Chl *a* (**Fig. 3g**, and **Fig. S13**). *Synechocystis* cells were distributed non-uniformly throughout IO-ITO, with the greatest cell density being observed near the top of the electrode. *Synechocystis* cells were distributed uniformly along the pillars of the SP-ITO, with a greater density of cells depositing on the base of the pillars. *Synechocystis* cells were also distributed uniformly along the pillars of the BP-ITO, with a higher density of cells observed on the branches of the pillars. Enlarged colourised SEM images showed the distribution of cells from the top view of the electrodes (**Fig. 3h**). The cells were more densely distributed on the SP-ITO compared to IO-ITO, but most densely distributed on the BP-ITO, forming patches of biofilms.

Bio-photoelectrochemical output

The overall bio-photoelectrochemical output was assessed using chronoamperometry under dark/light cycles with moderate light (λ_{680nm}: 1 mW cm^{-2}). A three-electrode configuration was employed with the *Synechocystis*-loaded electrode as the working electrode.

In the absence of an exogenous electron mediator, *Synechocystis*-loaded micropillar ITO electrodes produced characteristic photocurrent profile of *Synechocystis* biofilms (**Fig. 4a** and **Fig. S14**),[7] the features of which are still under investigation[37]. The addition of the commonly used membrane-permeable electron mediator 2,6-dichloro-1,4-benzoquinone (DCBQ) resulted in approximately 80, 100, and 110-fold increase for the IO-ITO, SP-ITO and BP-ITO

electrodes (**Fig. 4b**), respectively, compared to their corresponding unmediated photocurrents. The effect of the mediator was greater for the micropillar array electrodes, which indicated that many cells on the electrode scaffold were not directly wired. This could be attributed to the multi-layer of cells on the base of the electrode (**Fig. S11c**) or loosely attached cells on the periphery of the micro-branches (**Fig. S11d**). The mediated photocurrent densities for *Synechocystis*-loaded BP-ITO electrodes were twice those of IO-ITO electrodes of the same height ($p = 3.6 \times 10^{-3}$) (**Fig. 4b**).

The non-mediated photocurrent density was also assessed as a function of pillar height for the SP-ITO and BP-ITO electrodes (**Fig. 4c** and **Fig. S15**). The photocurrent density peaked at pillar heights of 600 µm (SP: 1.43 ± 0.04 µA cm^{-2}, BP: 1.87 ± 0.06 µA cm^{-2}, $p \leq 2.0 \times 10^{-3}$), with a drop observed for electrodes with 800 µm pillars. The drop was attributed to the mechanical instability at 800 µm, which may be the height limit of pillars printable by the aerosol jet printing method.

In this comparison study, *Synechocystis*-loaded BP-ITO electrodes at 600 µm pillar height produced the highest non-mediated photocurrents. In the presence of mediators, EQE measurements carried out using red (680 nm) light at 1 mW cm^{-2} for this electrode showed that 29 ± 1 % of the light was converted to current (158 ± 5 µA cm^{-2}, **Table S3**), which aligned well with the 40% calculated light absorption by cells immobilised on this electrode (**Fig. S8b**). This is 10-fold higher in efficiency than the cells-loaded IO-ITO electrodes under analogous lighting conditions[7].

To determine the maximum photocurrent output that could be generated using this electrode under more realistic conditions, we changed to a white light source and increased the intensity until maximum photocurrent output was observed at 3 mW cm^{-2}. Under 3 mW cm^{-2} white light, non-mediated photocurrent outputs of 1.91 ± 0.03 µA cm^{-2} and mediated photocurrents of 236 ± 10 µA cm^{-2} were observed (**Fig. 4d** and **Table S3**). This is an order of magnitude enhancement compared to previous benchmark photosynthetic biofilm systems and is within reach of the calculated theoretical photocurrent densities that could be achieved by living photosynthetic electrodes (lower estimate: 340 µA cm^{-2}). Considering that less than 40% of the incident light was absorbed by the cells (**Fig. S8**), further improvements to the system are still possible via changes to the electrode structure to increase cell loading and light utilisation.

Structure-activity relationships

Two sets of comparisons were carried out: (i) between three different electrode architectures made with the same ITO nano-materials, height and geometric area; and (ii) amongst libraries of micropillar ITO electrodes of different heights and surface roughness.

In the first comparison (**Fig. 5a** and **Fig. S14**), *Synechocystis*-loaded BP-ITO electrodes (50 µm height) yielded 2-fold higher mediated photocurrent densities than the *Synechocystis*-loaded IO-ITO electrode (50 µm height, $p = 3.6 \times 10^{-3}$) despite the IO-ITO structure exhibiting 21% higher EASA ($p = 1.4 \times 10^{-3}$). This implies that light flux into the bio-photoelectrode interface was limiting performance of the IO-ITO structure. *Synechocystis*-loaded BP-ITO electrodes resulted in mediated photocurrent densities of 31 ± 2 µA cm^{-2}, which was significantly higher than the 21 ± 2 µA cm^{-2} of SP-ITO electrodes ($p = 3.9 \times 10^{-2}$); this was attributed to the micro-branching resulting in a significant enhancements to EASA (23 %, $p = 4.0 \times 10^{-3}$).

In the second comparison, a Spearman's rank correlation matrix was calculated from the library of micropillar structures to identify correlations between the properties of these electrodes (**Fig. 5b**, **Fig. S16** and **Supplementary Note 3**). Significant and strong correlation was observed between the pillar height of electrodes and their EASA (R = 0.96, $p = 6.5 \times 10^{-7}$), transmittance (R = –0.79, $p = 2.16 \times 10^{-3}$), reflectance (R = 0.71, $p = 1.01 \times 10^{-2}$), Chl *a* loading (R = 0.96, $p = 6.5 \times 10^{-7}$) and photocurrent density (R = 0.86, $p = 3.09 \times 10^{-4}$). This implied that the larger surface of taller pillars provided more sites for cell loading and improved the trapping of light within the structure. No significant correlation was observed between pillar micro-roughness and the photocurrent density across the library, though significant differences were observed for pillars with heights between 100-600 µm (100 µm: $p \leq 2.0 \times 10^{-2}$). This suggested that the macroscale features of micropillar electrodes (in this instance, pillar height) were the most important consideration for boosting photocurrent output. However, significant correlations were observed between micro-roughness and reflectance (R = 0.63, $p = 2.89 \times 10^{-2}$); suggesting that micro-roughness was important for introducing favourable photonic effects (important for low light conditions).

Conclusion

We established a robust 3D printing methodology for generating micropillar array structures with multi-scalar hierarchical features using nanoparticles; the power of this method is that multi length-scale features can be tuned. This methodology can be applied to fields where electrode structural considerations are important for performance.

Our fabrication method enabled comparison studies to be performed over a large library of electrodes to identify the bottlenecks currently limiting bio-photoelectrodes. We demonstrated that although macroporous electrodes offered large EASA for high biocatalyst loading, light and electrolyte penetration was limited through the structure. The micropillar electrode design overcame this issue, and the addition of submicron-roughness to the surfaces boosted EASA, cell loadings and light harvesting. Applying the lessons from this study, future electrode design within the field of photoelectrochemistry should prioritise light flux considerations before introducing highly structured architectures to boost electron flux capacity.

The photocurrent outputs (up to 245 µA cm^{-2} for mediated electron transfer and up to 1.93 µA cm^{-2} for direct electron transfer) demonstrated here is a milestone in bio-photoelectrochemistry. It brings us one order of magnitude closer to the photocurrents needed for living photosynthetic cells to be competitive in bioenergy generation. For example, when this bio-anode is paired with an appropriate cathode to result in a typical voltage difference (0.213 V), power densities of 541 mW m^{-2} can be estimated - this already compares favourably against biofuel generation (< 403 mW m^{-2})[8]. Lessons from this study will guide the development of future high-performing bio-electrode structures; however, advancements to electron mediation strategies (to replace DCBQ, which exerts cytotoxicity and is unstable) will be important for long-term high performance[38]. This study demonstrates the power of 3D printing in 3D electrode design and opens new directions for understanding and enhancing the bio-electrode interface.

Acknowledgements

This work was supported by the Biotechnology and Biological Sciences Research Council (BB/M011194/1 to JML, BB/R011923/1 to JZ, and XC), the Cambridge Trust (LTW), the Isaac Newton Trust (SCHERTEL SNSF3 to LS). S.K.-N. is grateful for support from a European Research Council (ERC) Starting Grant (ERC-2014-STG-639526, NANOGEN). S.K.-N. and Q.J. S.K.-N. and Q.J. acknowledge support from the EPSRC Centre of Advanced Materials for Integrated Energy Systems "CAM-IES" (grant EP/P007767/1). We thank Henry Lloyd-Laney and Ezra Kitson for helpful discussions in statistical analysis. We thank Professor. Nicolas

Plumeré and Dr. Huaiguang Li for helpful discussions in electrochemistry. We thank Professor. Paulo J. Bártolo and Dr. Fengyuan Liu for helpful discussions in 3D bioprinting.

Author Contributions

JZZ and XC conceived the project and wrote the manuscript; XC was the lead experimenter, interpreted the data and produced Figures 1-4; JML helped with the preparation of the manuscript performed and interpreted the statistical analysis, and produced Figure 5b; LTW provided biological samples and expertise; LS helped to design and carry out and interpret the light transmission/reflection/absorption experiments; QJ helped to establish the initial protocol for aerosol jet printing pillars; SV helped guide the light experiments; CJH contributed biological expertise and samples; SK-N helped to guide the initial printing experiments. All contributed comments to the manuscript.

Competing Interests

The authors declare no competing interests.

Figures

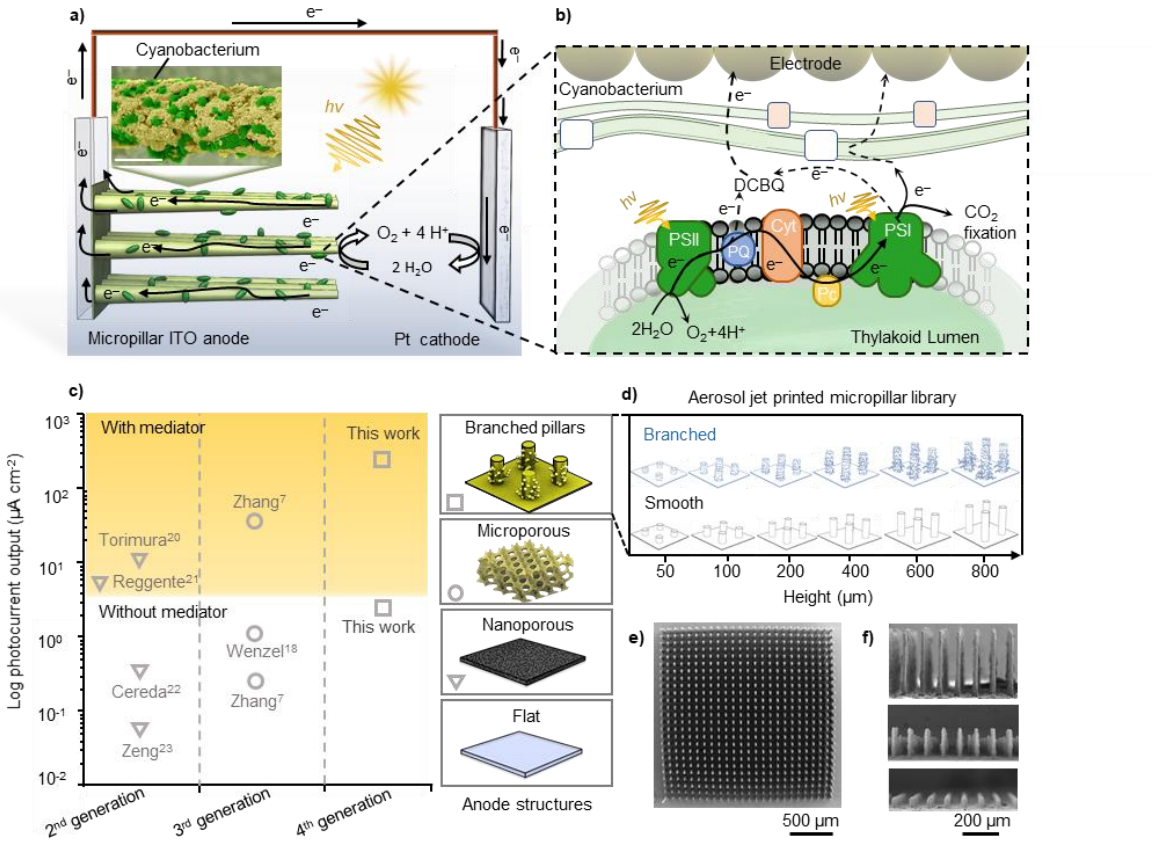


Figure 1: Next-generation electrodes for biophotoelectrochemistry. a) Schematic of a biophotoelectrochemical cell performing biological solar-electricity generation using photosynthetic biofilms as photocatalysts. Electron flux originating from photosynthetic water oxidation is harvested at the anode and transferred to a cathode, which reduces oxygen back to H_2O. Inset: colourized scanning electron microscopy (SEM) image of a micropillar with cyanobacteria adsorbed electrode printed from indium tin oxide (ITO) nanoparticles (scale bar: 10 μm). **b)** Schematic of the cyanobacterium-anode interface. Light is harvested by photosystem II (PSII), which is used to oxidise water resulting in the liberation of electrons, O_2 and H^+. The electrons are transferred through the photosynthetic electron transport chain to photosystem I (PSI), which pumps absorbed light energy into the electrons. The electrons can be used in a range of reductive pathways in the cell, including the Calvin-Benson cycle for CO_2 fixation. Some electrons from photosynthesis undergo extracellular electron transport, which can be enhanced by exogenous electron mediators such as 2,6-dichloro-1,4-benzoquinone (DCBQ), shuttling electrons to the electrode[6]. **c)** Photocurrent output from select key cyanobacterial-electrodes corresponding to different generations of electrode design[7,18 20-23]. **d)** The library of aerosol jet printed micropillar ITO electrodes library presented in this study. **e)**

SEM image of a printed micropillar array electrode (top view). **f)** SEM images of printed micropillar array electrodes (20 µm diameter, 100 µm spacing) of different heights (side view).

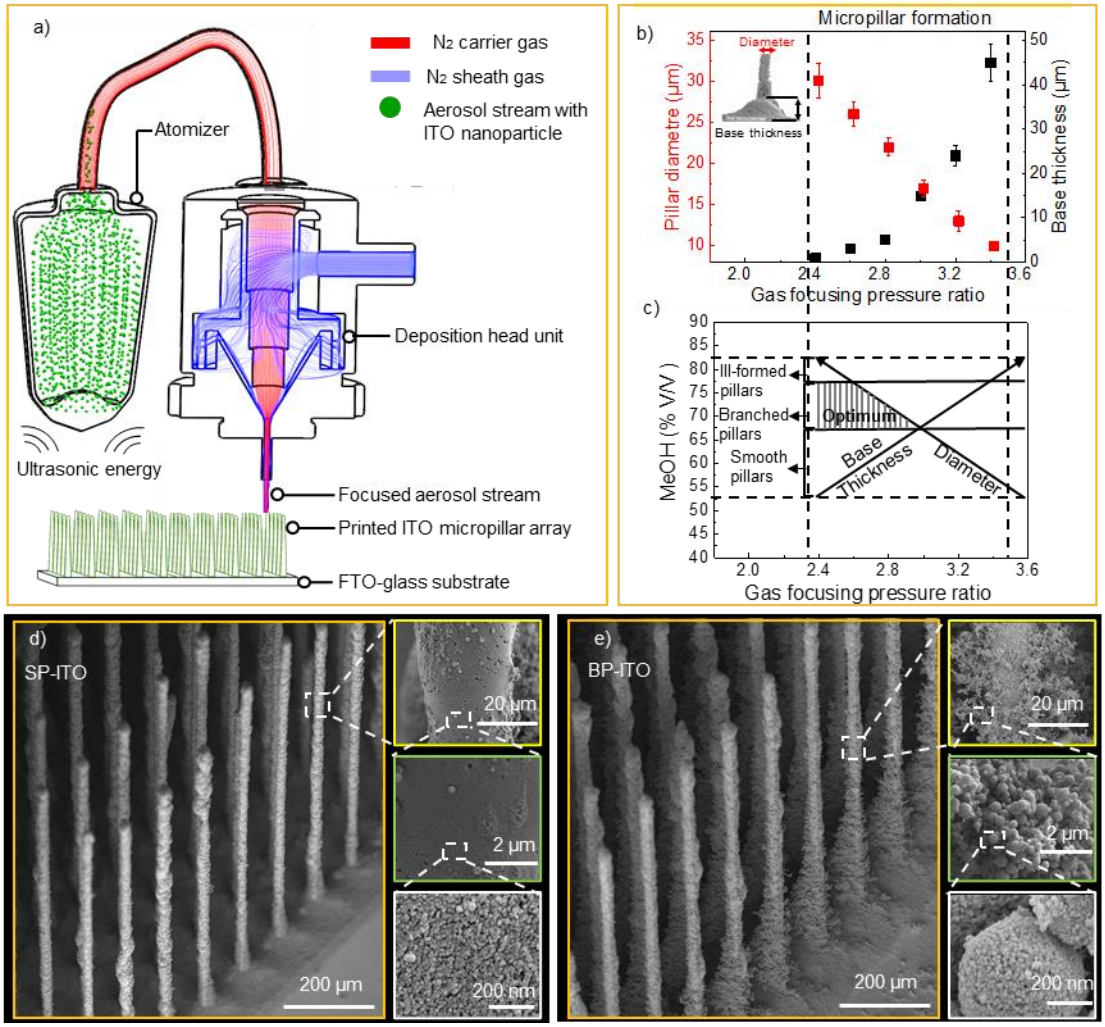


Figure 2: Aerosol jet printing of micropillar array electrodes. a) Schematic of the printing process. The ITO nanoparticle in methanol/water ink precursor was placed in an ultrasonic atomizer where it was aerosolized, entrained in a N_2 carrier gas stream, and aerodynamically focused via a stream of coaxial N_2 sheath gas. The micropillar ITO structures were printed onto a fluorine-doped tin oxide (FTO) coated glass. **b)** Printing parameters for producing micropillars: the gas focusing pressure ratio was identified as a key control parameter for tuning pillar shape. Inset: SEM image of a representative printed pillar with a base. **c)** Printing parameters for producing sub-micron roughness: an optimal operational window between gas focusing pressure ratio and ink MeOH content was identified to from micro-droplet branches. **d)** SEM image of a representative smooth micropillar ITO (SP-ITO) electrode with a height of 600 µm and diameter of 20 µm. Images obtained at higher magnifications show nano-features resulting from the packing of the nanoparticles. The SP-ITO was fabricated using a focusing

pressure ratio of 2.5 and MeOH volume fraction of 60%. **e)** SEM image of a representative branched micropillar ITO (BP-ITO) electrode with the height of 600 µm and diameter of 20 µm. Images obtained at higher magnifications show micro-branch features comprising submicron droplets. Further magnification of the droplet features shows nano-features of the nanoparticles. The BP-ITO was fabricated using a gas focusing pressure ratio of 2.5 and MeOH volume fraction of 70%. Error bars represent the standard error of the mean (n = 3).

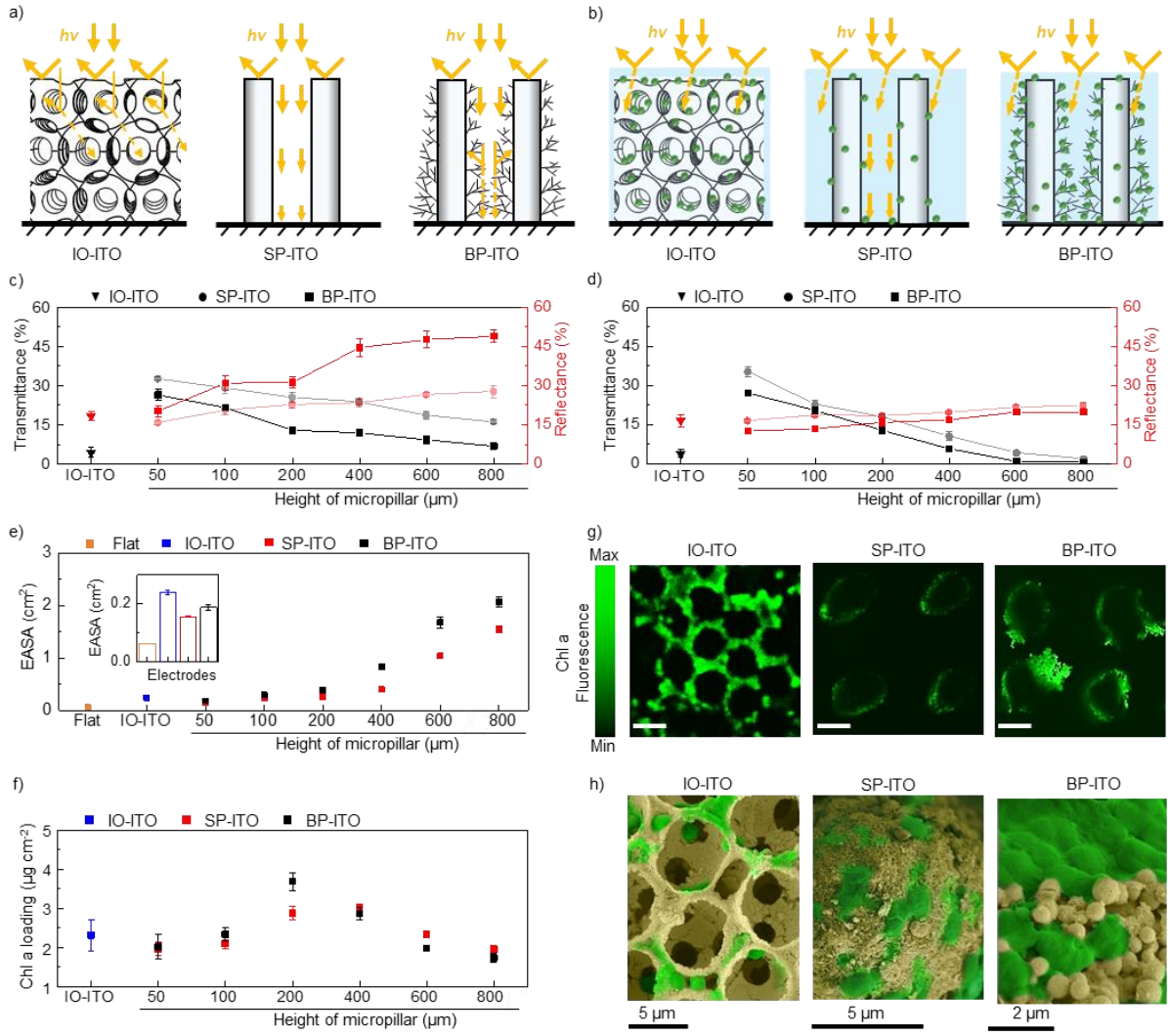


Figure 3: Printed micropillar electrodes exhibit high light transmission and cell loading. Light transmittance and reflectance studies of bare electrodes in air (**a** and **c**) and electrodes incubated with cells (**b** and **d**) using 0° vertical incident white light (1 mW cm^{-2}). The IO-ITO electrodes were 50 µm in height, the SP-ITO and BP-ITO electrodes ranged from 50 µm to 800 µm in height. Concentrated suspensions of *Synechocystis* cells (150 nmol (Chl *a*) mL^{-1} in BG11 medium) were incubated with electrodes for 12 h, the electrodes were gently washed with the fresh medium before measurements. **e**) Electroactive surface area (EASA) of flat, IO-

ITO, SP-ITO, and BP-ITO electrodes determined via capacitance measurements. Inset: zoomed in comparison of the EASA of flat, IO-ITO, SP-ITO, and BP-ITO electrodes all of 50 µm height. **f**) EASA-normalised Chl *a* loading on electrodes following 12 h incubation with *Synechocystis* and a gentle medium wash. **g**) Representative confocal microscopy images showing a cross-section through the middle of *Synechocystis*-loaded electrodes. Scale bar: 20 µm. **h**) Representative colourised SEM images of *Synechocystis*-loaded electrodes (top view). Error bars represent the standard error of the mean (n = 3).

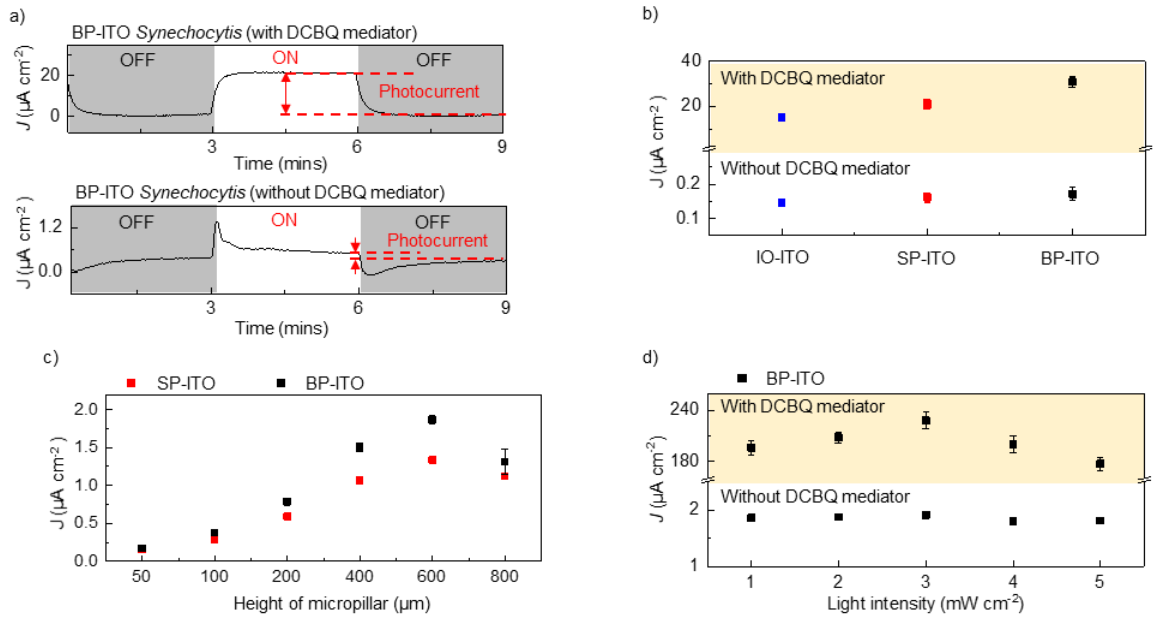


Figure 4: The photoelectrochemical performance of the *Synechocystis*-loaded electrodes. **a)** Representative photocurrent profile obtained from a *Synechocystis*-loaded BP-ITO electrode in presence and absence of the exogenous electron shuttle DCBQ (1 mM). **b)** Summary of mediated and non-mediated photoelectrochemical performances of *Synechocystis*-loaded electrodes with different electrode architecture at equivalent thickness (50 µm) under red light (680 nm, 1 mW cm^{-2}). **c)** Summary of non-mediated photoelectrochemical performances of the *Synechocystis*-loaded SP-ITO and BP-ITO electrodes with varying pillar heights without exogenous electron shuttles under red light (680 nm, 1 mW cm^{-2}). **d)** The photoelectrochemical performance of optimised *Synechocystis*-loaded BP-ITO electrodes (600 µm pillar height) under white light conditions of different intensities. Chronoamperometry experiments were performed with an applied potential of 0.3 V and 0.5 V vs SHE in the absence and presence of DCBQ, respectively, and in BG11 (pH 8.5) at 25 ºC. Error bars represent the standard error of the mean (n = 3).

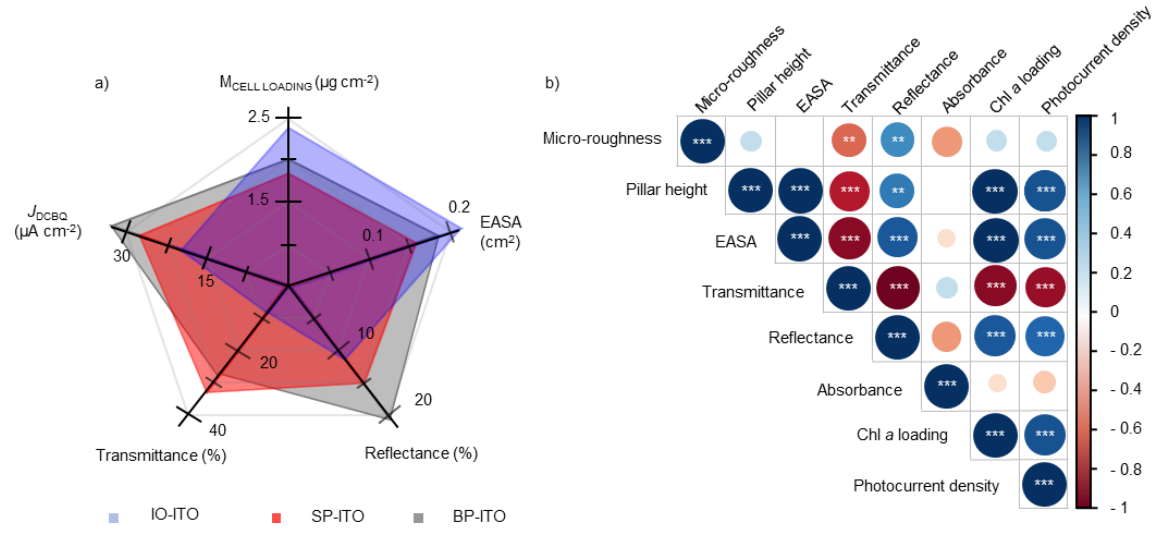


Figure 5: Structure-activity relationship analysis: **a)** Radar chart comparison between IO-ITO, SP-ITO and BP-ITO electrode structures (50 µm in height). **b)** Spearman's rank correlation matrix of micropillar electrodes and their properties. The scale bar represents the strength and sign of the correlation coefficient (R), with blue indicating a positive and red a negative correlation coefficient. Stars indicate significance where $*$ is $p \leq 0.1$; $**$ is $p \leq 0.05$ and $***$ is $p \leq 0.01$.

References

1 Kornienko, N., Zhang, J. Z., Sakimoto, K. K., Yang, P. D. & Reisner, E. Interfacing nature's catalytic machinery with synthetic materials for semi-artificial photosynthesis. *Nature Nanotechnology* **13**, 890-899, doi:10.1038/s41565-018-0251-7 (2018).

2 Zhang, J. Z. & Reisner, E. Advancing photosystem II photoelectrochemistry for semi-artificial photosynthesis. *Nature Reviews Chemistry* **4**, 6-21, doi:10.1038/s41570-019-0149-4 (2020).

3 King, P. W. Semi-synthetic strategy. *Nature Energy* **3**, 921-922 (2018).

4 Léger, C. & Bertrand, P. Direct electrochemistry of redox enzymes as a tool for mechanistic studies. *Chemical Reviews* **108**, 2379-2438 (2008).

5 Saar, K. L. *et al.* Enhancing power density of biophotovoltaics by decoupling storage and power delivery. *Nature energy* **3**, 75-81 (2018).

6 Wey, L. T. *et al.* The development of biophotovoltaic systems for power generation and biological analysis. *ChemElectroChem* **6**, 5375-5386 (2019).

7 Zhang, J. Z. *et al.* Photoelectrochemistry of Photosystem II in Vitro vs in Vivo. *Journal of the American Chemical Society* **140**, 6-9 (2018).

8 McCormick, A. J. *et al.* Biophotovoltaics: oxygenic photosynthetic organisms in the world of bioelectrochemical systems. *Energy & Environmental Science* **8**, 1092-1109 (2015).

9 Bradley, R. W., Bombelli, P., Lea-Smith, D. J. & Howe, C. J. Terminal oxidase mutants of the cyanobacterium Synechocystis sp. PCC 6803 show increased electrogenic activity in biological photo-voltaic systems. *Physical Chemistry Chemical Physics* **15**, 13611-13618 (2013).

10 Sekar, N., Jain, R., Yan, Y. & Ramasamy, R. P. Enhanced photo-bioelectrochemical energy conversion by genetically engineered cyanobacteria. *Biotechnology and bioengineering* **113**, 675-679 (2016).
11 Liu, C., Dasgupta, N. P. & Yang, P. Semiconductor nanowires for artificial photosynthesis. *Chemistry of Materials* **26**, 415-422 (2014).
12 Mersch, D. *et al.* Wiring of photosystem II to hydrogenase for photoelectrochemical water splitting. *Journal of the American Chemical Society* **137**, 8541-8549 (2015).
13 Wijnhoven, J. E. & Vos, W. L. Preparation of photonic crystals made of air spheres in titania. *Science* **281**, 802-804 (1998).
14 Liu, Y. *et al.* Macroporous indium tin oxide electrode layers as conducting substrates for immobilization of bulky electroactive guests. *Electrochimica Acta* **140**, 108-115 (2014).
15 Riedel, M. & Lisdat, F. Integration of enzymes in polyaniline-sensitized 3D inverse opal TiO2 architectures for light-driven biocatalysis and light-to-current conversion. *ACS applied materials & interfaces* **10**, 267-277 (2018).
16 Xia, L. *et al.* Zinc oxide inverse opal electrodes modified by glucose oxidase for electrochemical and photoelectrochemical biosensor. *Biosensors and Bioelectronics* **59**, 350-357 (2014).
17 Arsenault, E., Soheilnia, N. & Ozin, G. A. Periodic macroporous nanocrystalline antimony-doped tin oxide electrode. *Acs Nano* **5**, 2984-2988 (2011).
18 Wenzel, T., Härtter, D., Bombelli, P., Howe, C. J. & Steiner, U. Porous translucent electrodes enhance current generation from photosynthetic biofilms. *Nature communications* **9**, 1-9 (2018).
19 Fang, X., Kalathil, S., Divitini, G., Wang, Q. & Reisner, E. A three-dimensional hybrid electrode with electroactive microbes for efficient electrogenesis and chemical synthesis. *Proceedings of the National Academy of Sciences* **117**, 5074-5080 (2020).
20 Torimura, M., Miki, A., Wadano, A., Kano, K. & Ikeda, T. Electrochemical investigation of cyanobacteria Synechococcus sp. PCC7942-catalyzed photoreduction of exogenous quinones and photoelectrochemical oxidation of water. *Journal of Electroanalytical Chemistry* **496**, 21-28 (2001).
21 Reggente, M., Politi, S., Antonucci, A., Tamburri, E. & Boghossian, A. A. Design of Optimized PEDOT-Based Electrodes for Enhancing Performance of Living Photovoltaics Based on Phototropic Bacteria. *Advanced Materials Technologies* **5**, 1900931 (2020).
22 Cereda, A. *et al.* A bioelectrochemical approach to characterize extracellular electron transfer by Synechocystis sp. PCC6803. *PLoS One* **9**, e91484 (2014).
23 Zeng, Y. *et al.* Photoactive Conjugated Polymer-Based Hybrid Biosystems for Enhancing Cyanobacterial Photosynthesis and Regulating Redox State of Protein. *Advanced Functional Materials* **31**, 2007814 (2021).
24 Sturmberg, B. C. P. *et al.* Modal analysis of enhanced absorption in silicon nanowire arrays. *Optics Express* **19**, A1067-A1081 (2011).
25 Ali, M. *et al.* Nanostructured photoelectrochemical solar cell for nitrogen reduction using plasmon-enhanced black silicon. *Nature communications* **7**, 1-5 (2016).
26 Wang, K., Chang, Y.-H., Zhang, C. & Wang, B. Conductive-on-demand: Tailorable polyimide/carbon nanotube nanocomposite thin film by dual-material aerosol jet printing. *Carbon* **98**, 397-403 (2016).
27 Saleh, M. S., Li, J., Park, J. & Panat, R. 3D printed hierarchically-porous microlattice electrode materials for exceptionally high specific capacity and areal capacity lithium ion batteries. *Additive Manufacturing* **23**, 70-78 (2018).
28 Saleh, M. S., Hu, C. & Panat, R. Three-dimensional microarchitected materials and devices using nanoparticle assembly by pointwise spatial printing. *Science advances* **3**, e1601986 (2017).

29 Ćatić, N. *et al.* Aerosol-jet printing facilitates the rapid prototyping of microfluidic devices with versatile geometries and precise channel functionalization. *Applied Materials Today* **19**, 100618 (2020).
30 Jabari, E. & Toyserkani, E. Micro-scale aerosol-jet printing of graphene interconnects. *Carbon* **91**, 321-329 (2015).
31 Sukeshini, A. M. *et al.* Aerosol jet printing and microstructure of SOFC electrolyte and cathode layers. *ECS Transactions* **35**, 2151 (2011).
32 Kalio, A. *et al.* Development of lead-free silver ink for front contact metallization. *Solar energy materials and solar cells* **106**, 51-54 (2012).
33 Lu, S. *et al.* Flexible, print-in-place 1D–2D thin-film transistors using aerosol jet printing. *ACS nano* **13**, 11263-11272 (2019).
34 Hong, K. *et al.* Aerosol jet printed, Sub-2 V complementary circuits constructed from P-and N-type electrolyte gated transistors. *Advanced Materials* **26**, 7032-7037 (2014).
35 Lin, J.-T. *et al.* A high-efficiency HIT solar cell with pillar texturing. *IEEE Journal of Photovoltaics* **8**, 669-675 (2018).
36 Saini, D. K., Pabbi, S. & Shukla, P. Cyanobacterial pigments: Perspectives and biotechnological approaches. *Food and chemical toxicology* **120**, 616-624 (2018).
37 Wey, L. T. *et al.* A biophotoelectrochemical approach to unravelling the role of cyanobacterial cell structures in exoelectrogenesis. *Electrochimica Acta* **395**, 139214, doi:10.1016/j.electacta.2021.139214 (2021).
38 Clifford, E. R. *et al.* Phenazines as model low-midpoint potential electron shuttles for photosynthetic bioelectrochemical systems. *Chemical Science* **12**, 3328-3338 (2021).

Methods

Electrode fabrication

IO-ITO electrodes: The microporous electrodes (10 µm pores, ~ 3 µm channels, 50 µm thickness) were prepared using templated synthesis via an infiltration approach adopted from a previous study[7], with small adjustments. Briefly, cleaned FTO-coated glass (sheet resistance in 8Ω cm^{-2}, Sigma Aldrich) were applied with a mould in the form of a hole with geometric surface area 0.0625 cm^2 (prepared from electrical tape 25 mm thick). The FTO-coated glass with the attached mould was O_3 treated (UV/Ozone Procleaner, Bioforce Nanosciences) for 15 min. Polystyrene beads (10 µm diameter, 2.54% w/v suspension in water, Alfar Asaer) were spun down via centrifugation (12300 g, 5 min). The polystyrene bead sediments were re-suspended with supernatant using 1/4 of the original supernatant. Aliquots of the polystyrene bead suspension (30 µL) were spread inside the mould of the FTO-coated slides. To allow for uniform sedimentation, the polystyrene beads were slowly dried by evaporation over 3 h, followed by 10 mins sintering at 80 °C. ITO nanoparticles (80 mg, <50 nm diameter, Sigma Aldrich) were combined with a mixture of MeOH (252 µL) and deionized water (48 µL). The ITO suspension was ultrasonicated for 5 h at 50 ºC. The ITO suspension (6.8 µL) was dropcast

onto the polystyrene bead template and allowed to infiltrate slowly over approx. 1 h. The electrodes were annealed at 500 °C for 20 mins (ramp rate: 1 °C min^{-1}, carbolite furnace).

SP-ITO and BP-ITO electrodes: All micropillar structures were fabricated with an aerosol jet printer (AJ200, Optomec Inc.) using an ITO precursor (36 % w/v) prepared from a solvent mixture of water and MeOH. The ratio of water to MeOH was systematically changed from 6:1 to 1:6 to investigate the effect of solvent on pillar geometry formation. This ratio range is compatible with the ultrasonic atomizer with precursor viscosity no higher than 5 cP. The ITO ink precursor (2 mL) was ultrasonicated at 50 °C for 3 h prior to use. The ITO precursor was then transferred to the ultrasonic atomizer, which was maintained at a constant temperature of 14 °C using a water jacket.

The aerosol jet printer was situated inside a glovebox (MBRAUN) in an ultra-clean and highly purified gas environment with O_2 and H_2O concentrations < 1 ppm. Dry N_2 (HPCL grade, 99.998%) was used as the carrier gas of the ITO stream, which was set between 0-50 standard cubic centimetres minute (sccm). The focused sheath gas was set between 0-200 sccm, and the atomized current was maintained at 0.4 mA. The flowrates of the gasses were measured at their inlets of the printer. A 7.5 mm long nozzle with a diameter of 150 μm was used for printing. The electrodes were annealed at 500 °C for 20 mins (ramp rate: 1 °C min^{-1}, carbolite furnace).

More information on the operational mechanisms of the aerosol jet spray printing process can be found in the SI.

Electrode characterisation

SEM and EDX: SEM was conducted with a Tescan Mira3 FEG-SEM operated at an acceleration voltage of 5 kV. All the imaged samples were sputtered with a 10 nm layer of Pt to prevent charging. EDX was performed on Zeiss Auriga using 20 kV electron acceleration voltage, at a working distance of 5mm.

Transmission and reflection measurements: The electrode structures (IO-ITO, SP-ITO and BP-ITO) were sealed by a 3D-printed circular silicon mould (diameter: 1 cm, area = 0.75 cm^2, height: 3cm), covered by thin glass (thickness: 0.13 mm, Sigma Aldrich). This set-up is necessary to avoid the drying out of the pillar arrays, which could lead to collapsed pillars due to capillary load (**Figure S12**). A light source (Xenon lamp Ocean Optics HPX-2000) was coupled in an optical fibre (Thorlabs FC-UV100-2-SR) to illuminate the sample placed in front

(transmission) or at the back (reflection) of an integrated sphere (Labsphere). The scattered light was collected into an optical fibre which was connected to a spectrometer (Avantes HS2048) for the measurements (Fig. S4). For the transmission measurements, the illuminated light signal was normalized to the intensity (equivalent to 1 mW cm^{-2} at wavelength 680 nm) without samples. For the reflection measurements, the light signal was normalized according to the coating of the integrated sphere. FTO-glass (thickness: 3 mm, Sigma Aldrich) and cover-slip glass (thickness: 0.13 mm, Sigma Aldrich) were measured as the reference for both reflection and transmission tests. An unpolarized light was used with integration time of 2 s.

Electroactive surface area characterisation: The EASA was calculated from the capacitance of the electrodes, which was measure using cyclic voltammetry are different scan rates using the ITO electrodes as the working electrode, Pt mesh as the counter electrode and Ag/AgCl (KCl saturated) as the reference electrode. The electrolyte used was 1,1'-ferrocenedimethanol (1 mM in 1-butyl-3-methylimidazolium hexafluorophosphate). The capacitance was analysed using the equation (1) below:

$$\frac{i_a - i_c}{2} = Cv \quad (1)$$

Where C is the capacitance (F), i_a is the anodic current (A) measured at 0.3 V vs SHE, i_c is the equivalent cathodic current (A) measured at 0.3 V vs SHE and v is scan rate (V s^{-1}). An aerosol jet sprayed flat ITO surface (0.0625 cm^2) was used as the planar surface reference.

CVs at different scan rates were carried out with the intention of exploiting the Randle Sevcik equation to estimate the EASA using the peak currents of the 1,1'-ferrocenedimethanol. However, at high scan rates, quasi-reversible peaks were observed which precluded the use of this analysis method (see **Supplementary Note 4**).

Cell-loaded electrodes characterisation

Cell culturing: *Synechocystis sp.* strain PCC 6803 (Howe lab wild type strain) was grown photoautotrophically at 30 °C with a continuous white light intensity of 50 uE m^{-2} s^{-1} in BG11 medium supplemented with 10 mM $NaHCO_3$ [39]. Glycerol stocks were streaked onto agar plates (with solid medium containing 1.5 % agar). Individual colonies were picked to inoculate liquid cultures, which were air-bubbled and shaken at 120 rpm. Growth of liquid cultures was

monitored by attenuance (OD_{750}) with Chl *a* concentration determined by absorbances at 680 and 750 nm: (A_{680}-A_{750}) × 10.814[40].

The early stationary phase planktonic cultures (OD_{750} = 1) were centrifuged for 10 min at 5,000 g and resuspended in fresh BG11 to a concentration of 150 nmol Chl *a* mL^{-1} before photoelectrochemistry experiments.

Cell-loading on electrodes: A 3D-printed silicon circular mould (area = 0.75 cm^2) with height of 3 cm was used to surround the printed electrode structure on the FTO coated glass in a water-tight manner. Concentrated *Synechocystis* suspensions (30 µl, 150 nmol Chl *a* mL^{-1}) were pipetted into the silicon mould and allowed to incubate in the dark for 12 h. The mould functioned to decrease the rate of cell settling to the bottom of the electrodes. After 12 h, the cell loaded electrodes were carefully submerged with fresh BG11 to wash off loosely bound cells.

The cell loadings on the electrodes were determined using a previously reported method[7]. The concentration of Chl *a* loaded onto electrodes were typically measured immediately after photoelectrochemical or light transmission/reflection experiments. The cell-loaded ITO electrodes were scraped with a pipette tip from the substrate glass and into a microcentrifuge tube containing 500 µL MeOH. To avoid photodegradation of Chl *a*, the vial was covered with aluminium foil, then placed in an ultrasonic bath cooled to 0°C and sonicated for 30 min to extract all Chl *a*. The suspension was further centrifuged at 13,000 g for 3 min and the supernatant was analysed by UV-Vis spectrometry using the absorbance 665 nm and 750 nm: $\left(\frac{A_{665}-A_{750}}{79.95\ (Chl\ a\ mg)^{-1}\ mL\ cm^{-1}}\right)$

All UV-visible spectrophotometry measurements were made on a Varian Cary 50 Bio.

Confocal fluorescence microscopy: A Leica TCS SP8 confocal microscope with a 10x magnification objective was used to image cell attachment to the electrode structures following cell loading. A 633 nm laser (HeNe) was employed to excite biological cells, and the fluorescence was collected by a low-noise hybrid detector in the range of 650–750 nm. Z-stack images were acquired via sequential scanning downward from electrode surface to FTO glass substrate to the depth of 50 µm (Z-depth 0.5 µm).

Photoelectrochemistry: Photoelectrochemical experiments were carried out using an Ivium CompactStat potentiostat. A Pt mesh counter electrode and an Ag/AgCl (saturated KCl) reference electrode was used in combination with the cell-loaded ITO working electrodes. The

water-jacketed electrochemical cell was maintained at 25 °C and BG11 medium (pH 8.5) was used as electrolyte. A red LED light source (λ = 680 nm, THORLABS) at intensity of 1 mW cm^{-2} (which is equivalent to 56.8 µmol photons m^{-2} s^{-1}) was employed in the comparison studies. Chronoamperometry was carried out under light/dark cycles of 300 s on and 300 s off with an applied potential of 0.3 V (vs SHE) used in the absence of an exogenous electron mediator, and 0.5 V (vs SHE) used in the presence of DCBQ (1 mM). Where stated, a white LED light source (THORLABS, SM2F32-A) was also employed, and light-responses were tested at intensities that varied from 1 to 5 mW cm^{-2}. All chronoamperometry experiments were given 90 s of equilibrium period in the dark prior to initial light irradiation. It should be noted that in the presence of DCBQ, the mediated photocurrents drop rapidly, possibly due to diffusional limitations of the mediator in the unstirred electrolyte and partial cytotoxicity effects[41,42]. As such, only the initial (first light cycle) mediated photocurrents were analysed.

EQE Calculations: EQE is calculated based on percentage of incoming photons converted to electrons at a certain bias potential and can be calculated by equation listed below:

$$\text{EQE (\%)} = \frac{123.98J\ (\mu A/cm^2)}{[\lambda\ (nm)][I(mW/\ cm^2)}$$

Statistical analysis: Single-tailed ANOVAs were performed using the Data Analysis ToolPak in Microsoft Excel to calculate p-values when comparing experimental data, using a significance threshold of $p \leq 0.05$. `Correlation analysis was performed in the R environment (v4.0.4)`[43]. Quantitative data of electrodes were expressed as means (n =12). Micro-roughness was expressed as a binary integer (0 = SP-ITO, 1 = BP-ITO). Pairwise Spearman's rank correlations and p-values were calculated and visualised as a correlation matrix using the 'corrplot' package[44]. See **Supplementary Note 3** for a tutorial explanation of this analysis. The data and code used in the correlation analysis are available via the Apollo repository (DOI: 10.17863/CAM.80096) or on Github (https://github.com/JLawrence96/MicropillarArrayElectrodes).

Data Availability

All data and code used in this paper are via the Apollo repository (DOI: 10.17863/CAM.80096) or on Github (https://github.com/JLawrence96/MicropillarArrayElectrodes).

References for Methods

39 Stanier, R. Y., Kunisawa, R., Mandel, M. & Cohen-Bazire, G. Purification and properties of unicellular blue-green algae (order Chroococcales). *Bacteriological reviews* **35**, 171 (1971).

40 Lea-Smith, D. J. *et al.* Thylakoid terminal oxidases are essential for the cyanobacterium Synechocystis sp. PCC 6803 to survive rapidly changing light intensities. *Plant physiology* **162**, 484-495 (2013).

41 Yang, C., Zhou, E., Miyanishi, S., Hashimoto, K. & Tajima, K. Preparation of active layers in polymer solar cells by aerosol jet printing. *ACS applied materials & interfaces* **3**, 4053-4058 (2011).

42 Fang, X. *et al.* Structure–activity relationships of hierarchical three-dimensional electrodes with photosystem II for semiartificial photosynthesis. *Nano letters* **19**, 1844-1850 (2019).

43 Team, R. C. R: A language and environment for statistical computing. (2013).

44 R package “corrplot”: Visualization of a Correlation Matrix (Version 0.84). (2017).